Electronic Supplementary Material (ESI) for Nanoscale.

Supplementary Information

Spectral Triangulation: a Novel 3D Method for Localizing Single-Walled Carbon Nanotubes *in vivo*

Ching-Wei Lin[†], Sergei M. Bachilo[†], Michael Vu[¶], Kathleen M. Beckingham[¶] and R. Bruce Weisman[†,‡,*]

[†]Department of Chemistry and the Smalley-Curl Institute, [‡]Department of Materials Science and NanoEngineering, and [¶] Biosciences at Rice, Rice University, 6100 Main Street, Houston, TX 77005, USA

Contents

Preparation of tissue phantoms and mouse phantoms

Our optical tissue phantom material consists of 2% agar, 1% Intralipid (Sigma, cat. # I141) and 20 μM bovine hemoglobin (Sigma, cat # 08449) in PBS buffer. Two grams of agar was initially dissolved in 75 mL of hot water and allow to cool to approximately 60 °C. Then 10 mL of 10x stock solution of hemoglobin and PBS plus 5 mL of 20% Intralipid were mixed thoroughly with the agar solution. The tissue phantom solution was quickly poured into the mold (for plates or mouse shaped phantoms), and allowed to polymerize at room temperature.

To cast tissue phantoms in the shape of mice, we used the carcass of a hairless laboratory mouse to make a silicone rubber mold. After freezing, the mouse was lightly coated with a mold-release agent and placed ventral side down in a round container. Then plaster was added until the mouse carcass was half submerged. After approximately two hours, the mouse was carefully removed and the plaster mold was left overnight at room temperature to set completely. A thin coating of mold release agent was then applied to the wall of the plaster mold and it was filled with an epoxy-based matrix and cured for several days at room temperature. Then we carefully chiseled off the plaster from the epoxy mouse model. Finally, we made a silicone rubber impression of the epoxy mouse model using the materials and procedure in the EasyMold Kit (Fields Landing, CA). Once the silicone rubber had cured for 24 h, the epoxy model was removed, leaving a mouse mold suitable for casting optical phantoms. These steps were repeated to make a dorsal mold of the same mouse.

Design of SWCNT-scanner

Overview. The design principles and main scheme of the SWCNT-scanner are described in the main text. Here, we describe the design details of the instrument. Figure S1a shows a 3D diagram of the positioner built from a modified 3D printer. The specimen illuminator is embedded inside the platform under a fused silica window. The size of the illuminator LED matrix is ~5 × 5 cm, which is sufficient to cover a normal laboratory mouse. We removed the print head from the 3D printer and replaced it with our home-built contact probe. This probe collects SWCNT fluorescence and transmits it to the detectors through a 1 meter long step-index, low-OH optical fiber with a 400 μm core diameter (Thorlabs M28L01). We cover the plastic jacket of this optical fiber with aluminum foil to prevent infiltration of small amounts of room light, which otherwise gives a background signal when using the APD detector.

Contact probe. The threaded SMA collar at the specimen end of the optical fiber was removed to make it more compact and suitable for use as a probe. We installed a spring-loaded stainless steel tube around and protruding from the ferrule such that the barrel could slide smoothly. When the probe just contacts the surface of a specimen, the barrel retracts and closes a circuit by touching a wire mounted on the assembly. This sends a TTL signal to the positioning system's microcontroller, commanding a stop to vertical motion. After data acquisition at that position is complete, the probe is raised and translated to another position x,y position, where it again lowered to touch the specimen surface and collect optical data. An 800 nm long-pass dielectric filter is mounted over the probe tip to attenuate excitation light entering the probe. This suppresses the generation of SWIR fluorescence in the optical fiber and absorptive filters. An optical scatter plate made from Teflon tape is normally mounted in front of the long-pass filter to increase the effective numerical aperture of the optical fiber and reduce angular selectivity.

Illuminator. Figure 1c shows the design of our optical excitation system. The bottom layer is an aluminum cooling plate with an internal cooling channel. Chilled water at 20 °C was circulated through this channel at a flow rate of 12 mL/s to allow dissipation of more than 300

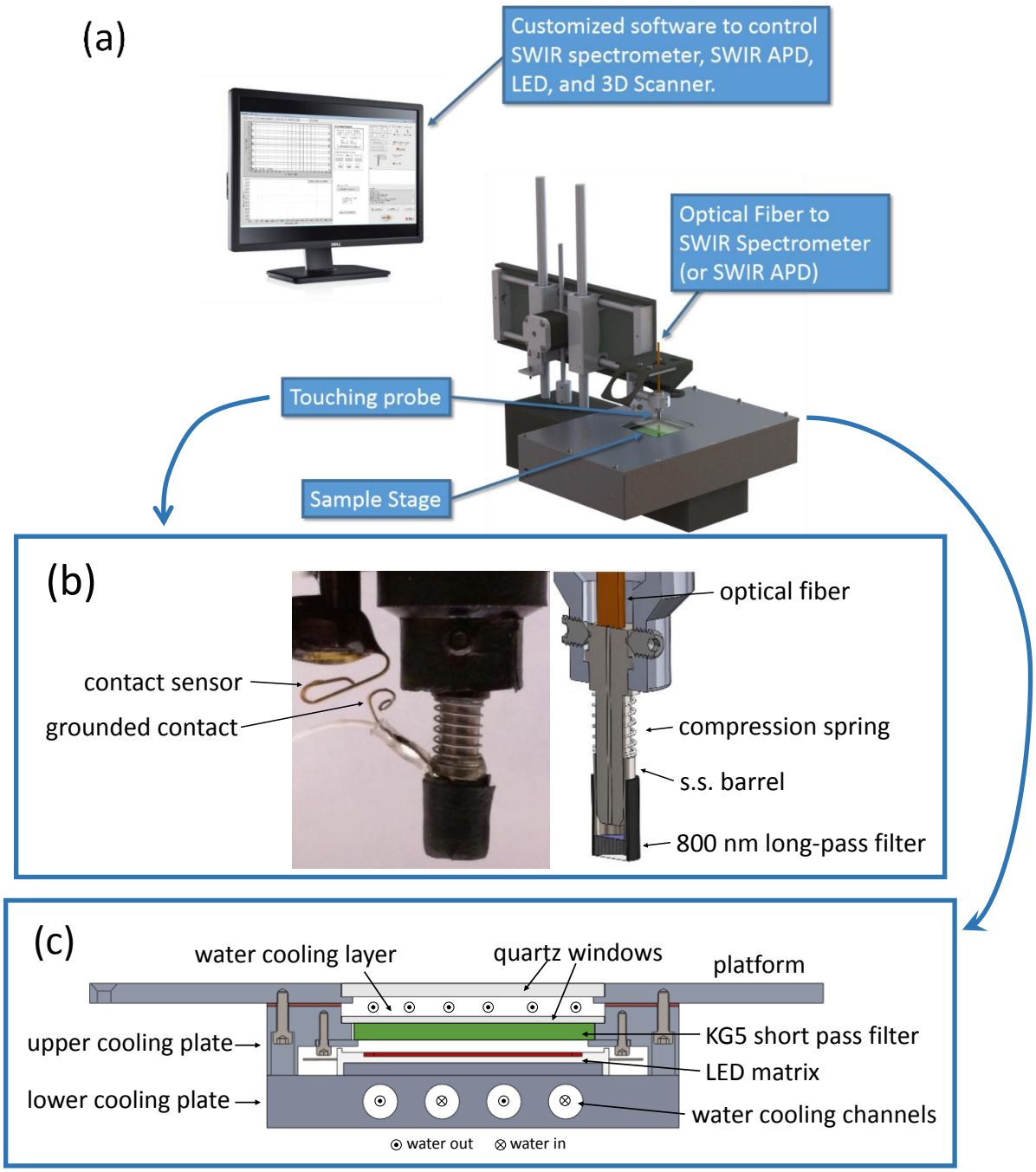

Figure S1. (a) 3D picture of modified 3D printer including LED, platform, contact probe, optical fiber and custom software. (b) Picture and 3D model of contact probe. (c) LED embedded platform.

W. A water layer between the surface of the specimen platform and the KG5 short-pass absorptive filter dissipates heat deposited in the KG5 filter and cools the specimen platform. Blackbody radiation above 1400 nm from the KG5 is also absorbed by this water layer, helping to suppress SWIR backgrounds. All insulating windows are fused silica rather than glass in order to prevent luminescence from inorganic impurities. We measured power densities from the LED matrix at the specimen platform using an optical power meter (Thorlabs S130C with PM200).

Motorized filter wheel. Figure S2 shows a 3D illustration of the filter wheel assembly. A 1" filter wheel plate (Thorlabs FW1AB) was attached to the shaft of a small stepper motor. SWCNT fluorescence emerging from the optical fiber is collimated, sent through the selected filter, and then focused into an output optical fiber. The filter choices are 850 nm long-pass (LP850), 1020 nm band-pass with 20 nm width (1020RDF20), and 1200 nm long-pass (1200LP). Filter wheel motion is controlled by the custom LabVIEW program. To ensure prompt start of data acquisition after the filter wheel motion is finished, an optoelectronic sensor monitors the filter wheel position. The sensor is also used to initialize the filter wheel position.

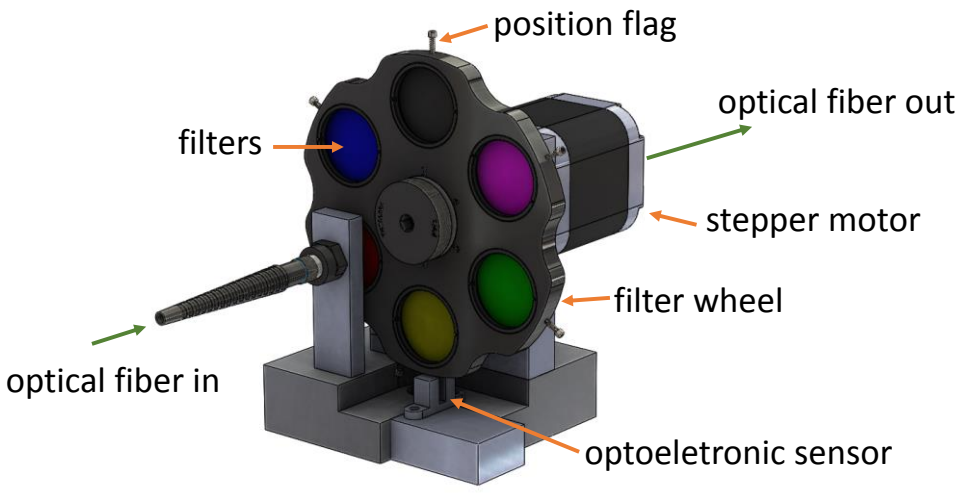

Figure S2. A 3D model for motorized optical filter wheel.

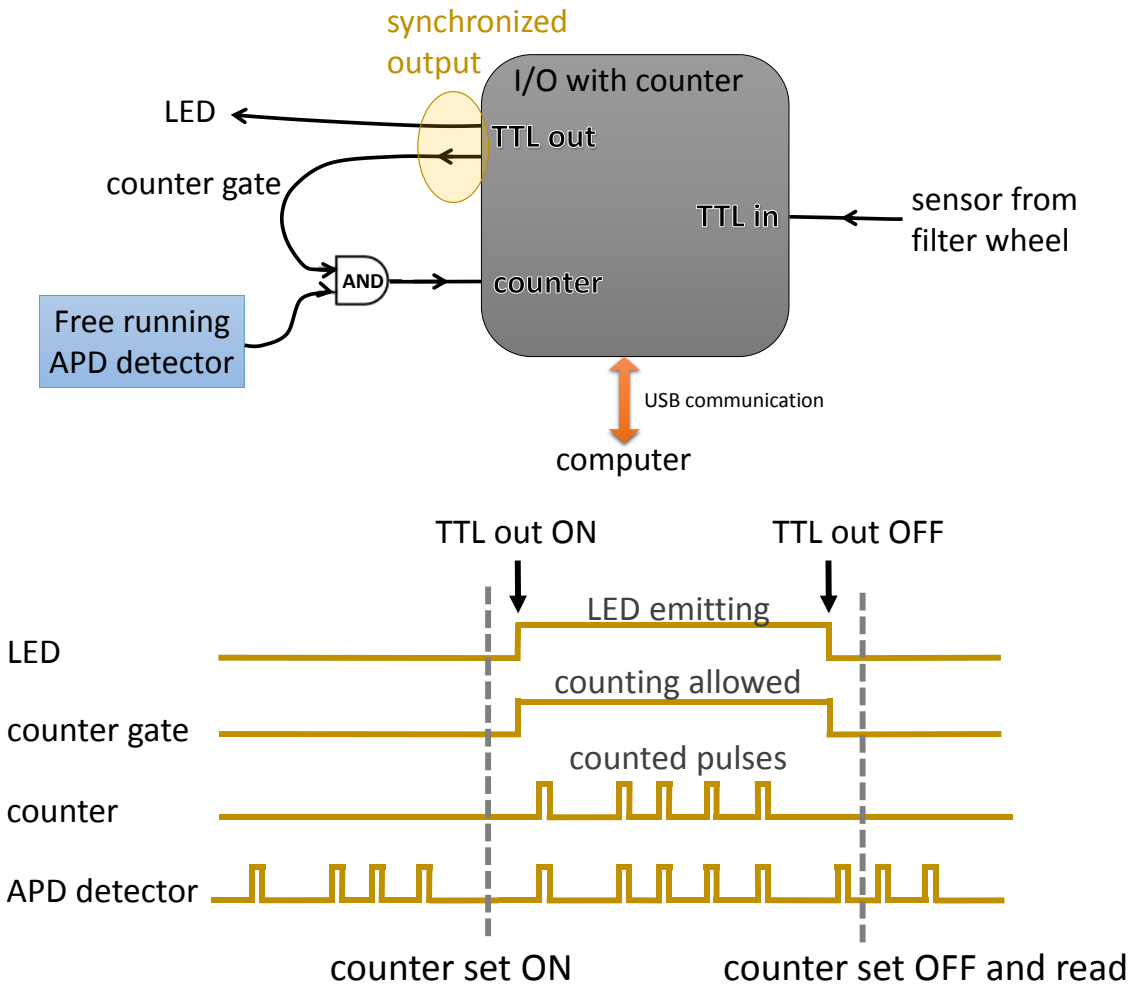

Figure S3. Device control and signal synchronization.

APD counting and synchronization. Following the filter wheel, SWIR emission is detected by a free-running mode InGaAs APD (ID Quantique model ID220) operated at -50 °C. As diagrammed in Figure S3, the APD output pulses are counted through a TTL AND gate synchronized with the specimen excitation. A computer-controlled I/O interface device (NI USB-6501) provides counting and digital input/output functions. Power to the LED matrix was switched by a Darlington transistor (2N6044) controlled by a TTL output line, and one of the TTL inputs is connected to the filter wheel position sensor.

LED excitation spectrum

Figure S4 shows the spectrum of the LED excitation matrix, as measured using the visible spectrometer of a model NS2 NanoSpectralyzer. The peak intensity is near 630 nm and the full width at half maximum is 13 nm. The peak is slightly asymmetric with a tail to shorter wavelengths.

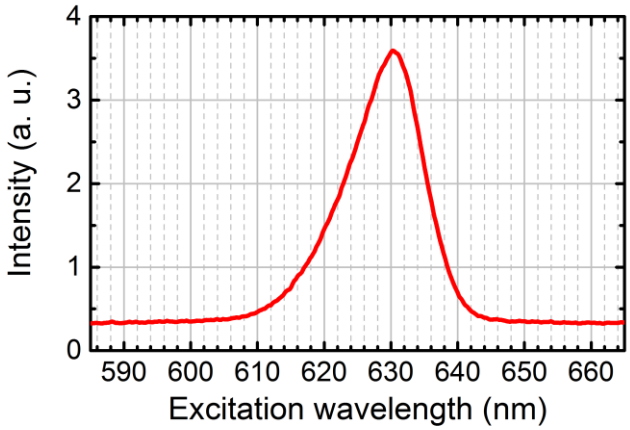

Figure S4. Spectrum of LED light used for SWCNT excitation.

Fluorescence and absorption spectra of SWCNTs

Figure S5a shows the absorption spectrum of the SWCNT suspension used in this study. Its preparation is described in the main text. Figure S3b shows the fluorescence spectrum of the SWCNT sample excited by LEDs at 630 nm. The absorption spectrum was measured using a prototype model NS2 NanoSpectralyzer, and the emission spectrum was measured directly through the SWCNT-scanner with 630 nm excitation.

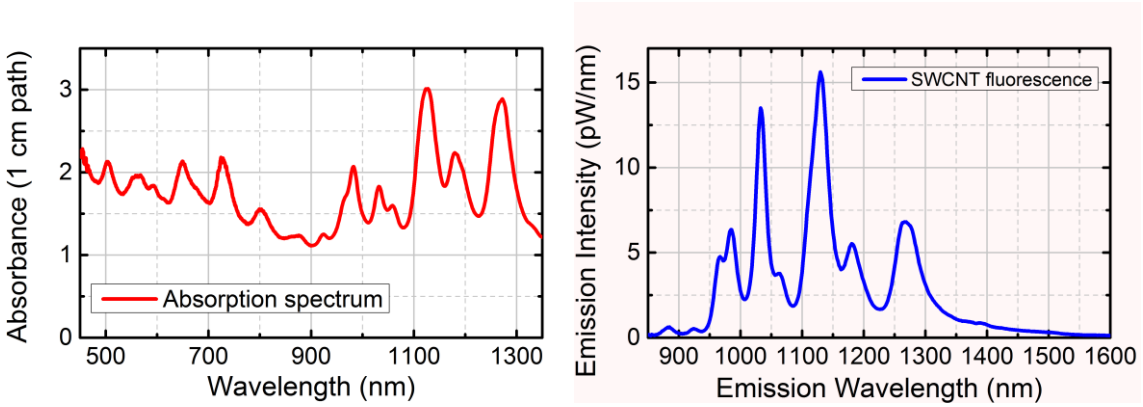

Figure S5. Absorption and fluorescence spectra of the SWCNT sample used for this study. The fluorescence excitation wavelength was 630 nm.

Loss of spatial resolution when imaging through tissue phantoms

The emission scan data plotted in Figure S6 show how images of a structured emitter lose spatial resolution as the light passes through increasing thicknesses of turbid optical media. The SWCNTs were confined to a cross-shaped channel, which can be clearly seen through 1-2 mm thick phantoms. However, the image degrades to a blurred round shape as thicker phantoms are used. In this project we have instead emphasized wavelength-dependent attenuation as a tool for deducing coordinates of emissive centers deeper inside turbid media.

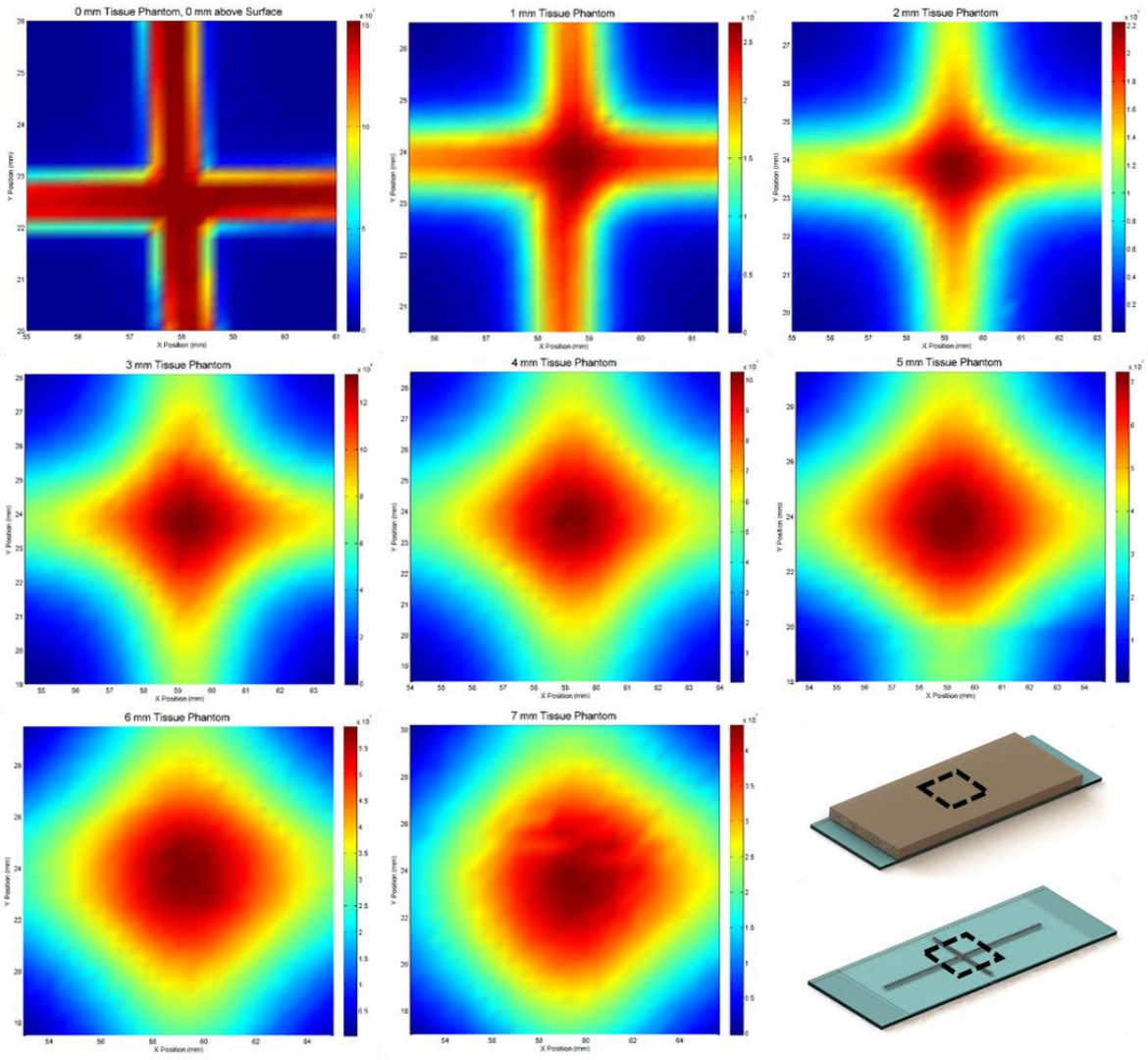

Figure S6. The loss of spatial resolution due to scattering. Tissue phantom thicknesses varied from 0 mm (top left frame) to 7 mm (bottom middle) in steps of 1 mm.

Signal-to-noise ratio comparison

The APD detector is theoretically much more sensitive than a normal photodiode array used in modular spectrometers. Here, we directly compared the BWTEK Sol 1.7 InGaAs spectrometer cooled to -15 °C with the ID Quantique InGaAs APD cooled to -50 °C. A stable SWCNT suspension was used as a SWIR fluorescence source. The SWCNT fluorescence was filtered by an 1120 nm band pass filter, so only photons with wavelength near 1120 nm reached the detectors. As shown in the Figure S7 inset, the spectrometer detected a small peak, covering about 15 channels, which we spectrally integrated (from 1112.4 to 1136.0 nm) for comparison to the APD signals. A set of 500 sequential acquisitions of 1 s each was made for the sample and again for a background without SWCNTs present. The set of measurements is plotted in Figure S7. S/N ratios were determined as the mean (sample – background) signal divided by the

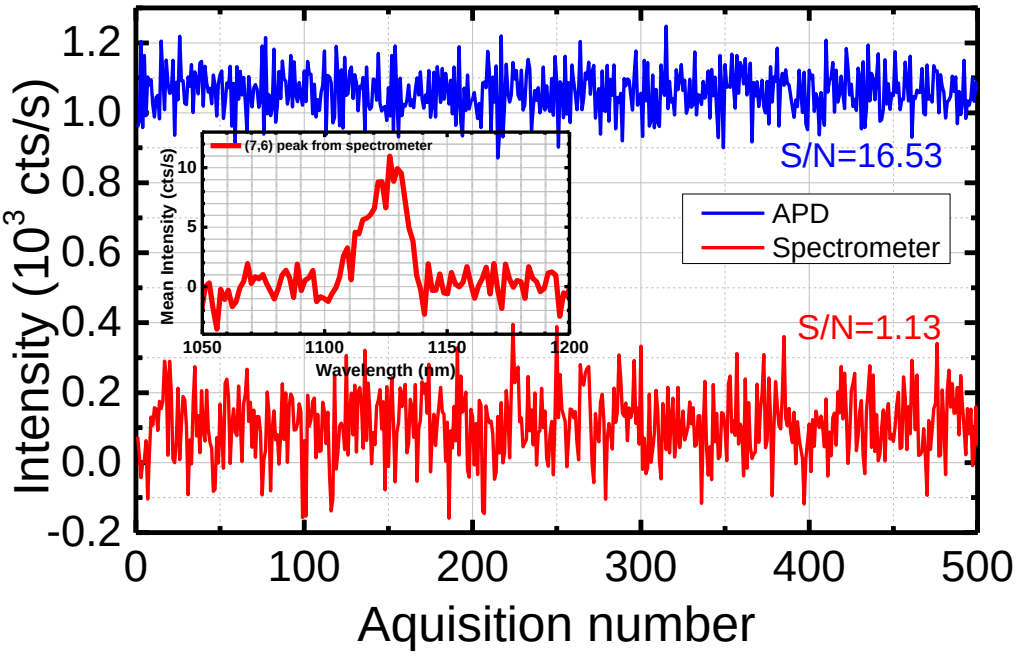

Figure S7. Signal to noise ratio (S/N ratio) comparison between BWTEK spectrometer and IDQ APD. Result shows the S/N ratio of APD is about 15 times higher than BWTEK spectrometer.

standard deviation. We found S/N ratios of 16.53 for APD detection and 1.131 for the spectrometer, giving a factor of 15 advantage for the APD. To achieve equal S/N ratios, a spectrometer detection experiment would thus require 15^2 or 225 times longer data averaging. Accounting for the use of two different spectral filters with APD measurements, the time advantage factor is reduced to 112.

Measurement of the contact probe acceptance angle

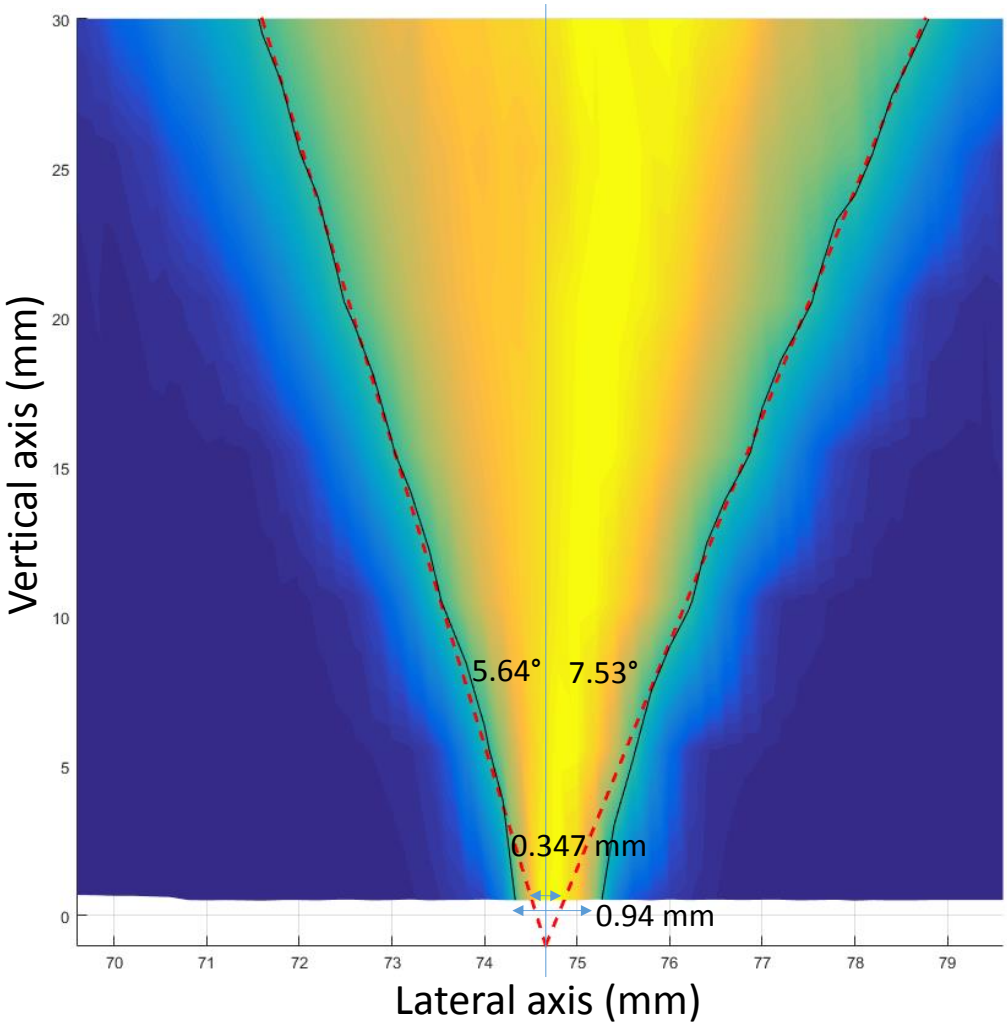

Figure S8. Measurement of numerical aperture of the contact probe. Colors code for intensities as a function of height above surface and lateral position (note different scale factors). The FWHM acceptance angle is approximately 13 degrees, corresponding to a numerical aperture of 0.115.

Because of the limited numerical aperture of the optical fiber and the detectors, light incident beyond the acceptance angle will not be registered. Figure S8 shows data measured to determine the acceptance angle of our system. SWCNT fluorescence went through a round aperture with 1 mm diameter. The probe was then scanned in the horizontal plane at various heights above the aperture, and signals were captured by the SWIR spectrometer. Lines corresponding to half-maximum intensities positions were drawn and fitted to obtain separate cone angles for each side. At the surface position, the extrapolated hole size was 0.94 mm, which is very close to the actual 1 mm physical size. The full acceptance angle at half-maximum is 13.2 degrees, corresponding to a numerical aperture value of 0.115.

Comparison of fluorescence attenuation between probe with and without scatter plate

The finite acceptance cone limits collection of light propagating at angles to the probe axis (see Figure 4b). Therefore, the fluorescence attenuation can depend not only on distance between SWCNT and probe but also on the angle. Figure S9 shows intensity as a function of source-to-probe distance as measured at several different positions on tissue phantom surfaces with thicknesses between 1 and 10 mm. In the top left frame, the black curve represents collection at the same lateral position as the SWCNT source (vertically above it), whereas

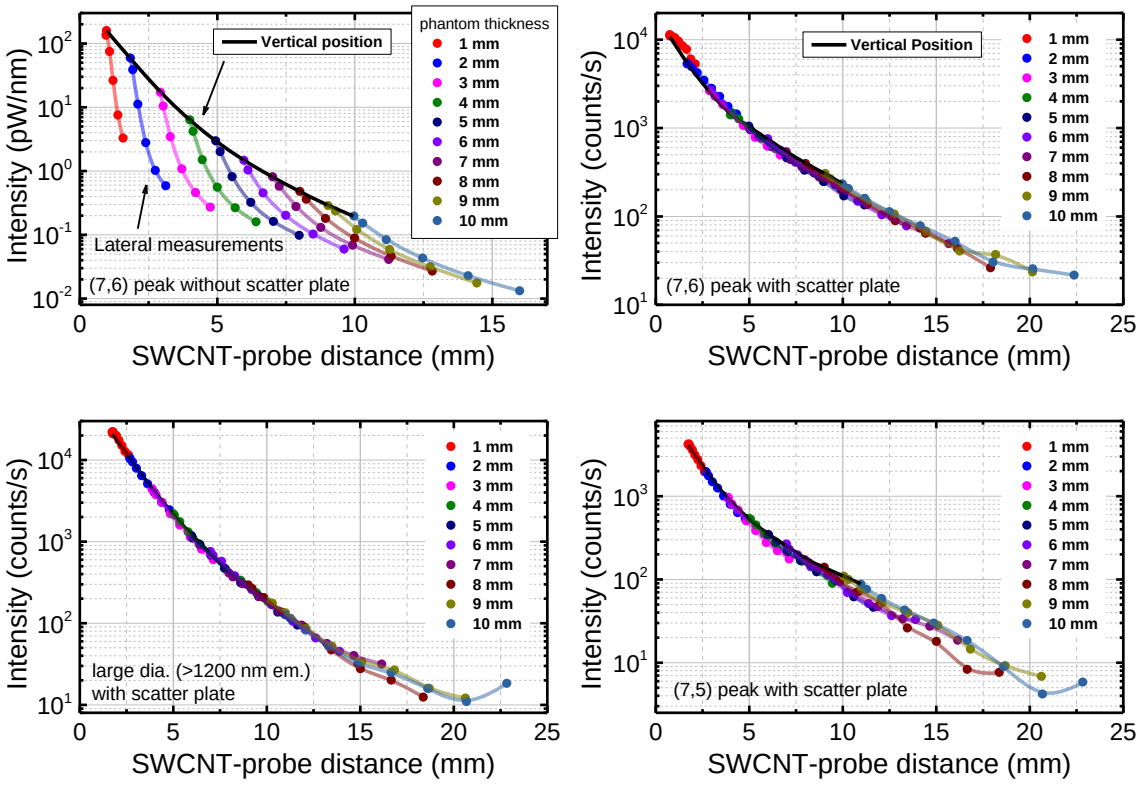

Figure S9. Effectiveness of Teflon scatter film in reducing angular sensitivity. (top left) Without scatter film, fluorescence signal from (7,6) peak depends strongly on both path length and angle. With scatter film in place, fluorescence signals depend only on path length: (top right) from (7,6) SWCNTs measured through 1120 nm band-pass filter; (bottom left) with 1200 nm long-pass filter; (bottom right) from (7,5) SWCNTs measured through 1020 nm band-pass filter.

colored curves show the fluorescence signals measured with the probe displaced laterally from the source with different phantom thicknesses. The large mismatches between the black and colored curves reveal a strong angular dependency of collection efficiency, particularly with thinner tissue phantoms in which scattered photons are less dominant. As described in the main text, we installed a Teflon scatter film over the collection fiber in an attempt to suppress these mismatches. The top right frame of Figure S9 shows comparable data to the top left frame, but with the scatter film in place. Here there is very satisfactory overlap of the black and colored curves, indicating successful removal of nearly all angular dependency. Similar results for other spectral channels detected through the scatter film are plotted in the two lower frames of the figure. We note that the slightly higher values obtained with the 1 mm tissue phantom reflect the deviation from point-source behavior of our 1 mm diameter SWCNT sample at this close range.

Intensity difference between probes with scatter film and without scatter film

Even though the Teflon scatter film essentially eliminates the angular dependency, it also reduces detected intensities. To quantify this loss, we scanned the fluorescence profiles using probes with and without the scatter film. The size of the SWCNT source was about 1 mm in diameter. Because we used a capillary tube as the SWCNT container, the fluorescence image appears slightly elongated along the capillary tube axis. Figure S10 plots the difference intensity between the two measurements, which is $I_{\text{diff}} = I_{\text{sca}} - I_{\text{non-sca}}$. I_{diff} larger than zero means the intensity with film is higher than the intensity without film. The red curve marks locations where this difference is zero because the two intensities are the same. The diameter of the red curve is

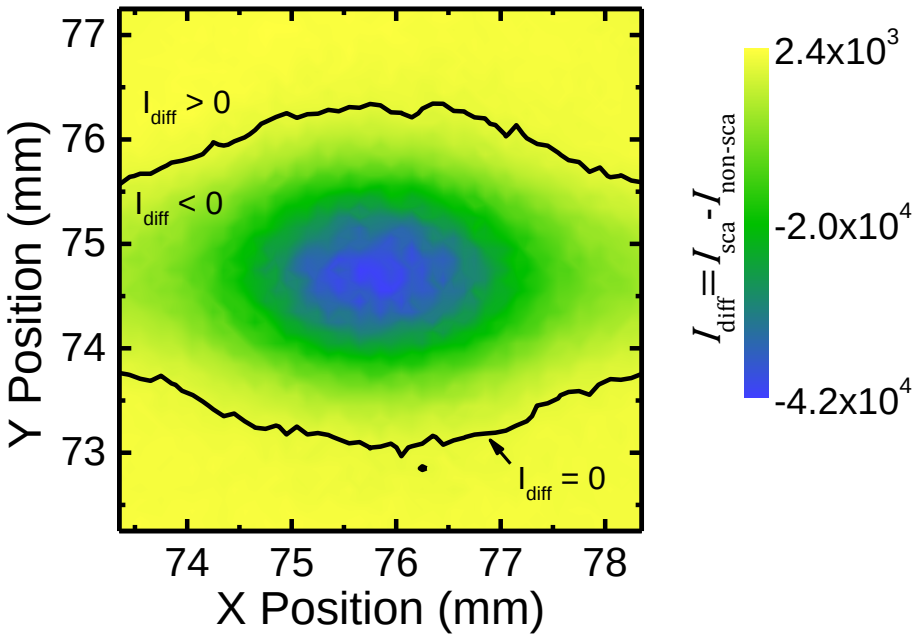

Figure S10. Intensity difference between probes with and without the scatter film.

~3.28 mm, which means the measured intensity is higher when the probe is laterally more than 1.64 mm away from the SWCNT source. The effect of the scatter film is to expand the lateral region over which fluorescence is detected while reducing the detected intensity near the source position.

Raw attenuation curve before normalization

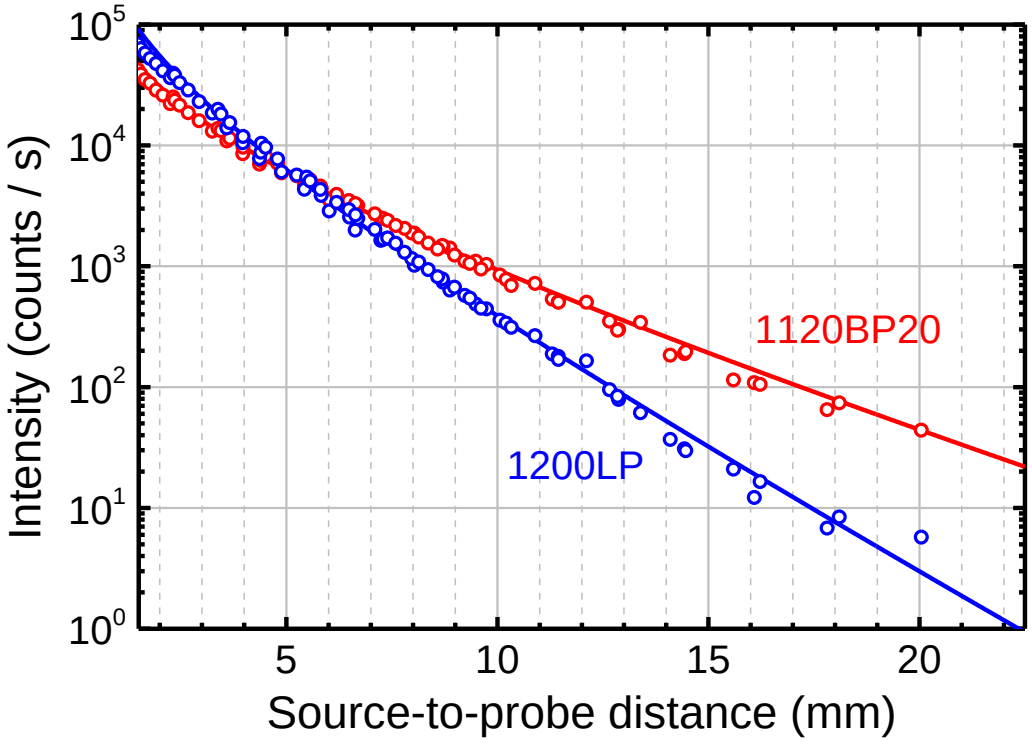

Figure S11. Attenuation curve data before normalization to obtain Figure 4c in the main text. This plot shows photon counts per second after subtraction of the APD dark count rate of ~600 counts/s with the 1120 nm band-pass filter and the 1200 nm long-pass filter.

Protocol for calibrating location of SWCNT source

In order to accurately calibrate the fluorescence attenuation function, it is necessary to know the exact position of the SWCNT source. We first did an x-y probe scan directly above the bare SWCNT source (without tissue phantom). The scan center position was set to approximately the position of SWCNT. Then a finer x-y scan was performed over a 2 mm by 2 mm area with 0.1 mm steps. At each grid point we used a 300 ms acquisition time. The resulting intensity data were fit with a 2D Gaussian profile $I(x,y) = a \cdot \exp\left\{-\left[\frac{(x-b)^2}{2c^2} + \frac{(x-d)^2}{2e^2}\right]\right\}$. The source lateral position was thereby found to be $(x_0, y_0) = (b, d)$. To find the z-coordinate of the source, the probe was moved to (x_0, y_0) and then lowered to make physical contact. Since the SWCNT source was sealed in a 2 mm OD quartz capillary tube, the z-axis center position of SWCNT source was taken as the measured z value minus 1 mm. Figure S11 shows the scanned intensity profile and its Gaussian fit.

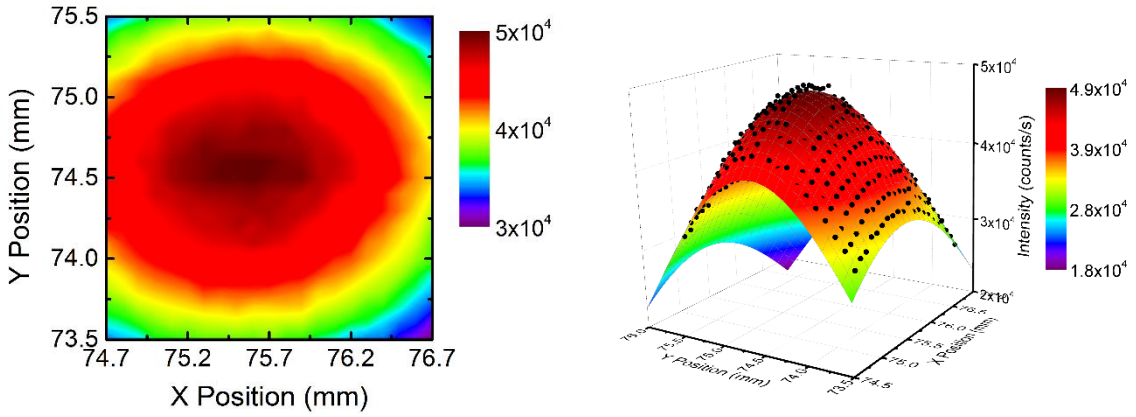

Figure S11. (a) Lateral scan of SWCNT source. (b) Data was fitted with a 2D Gaussian profile in order to find the center coordinates of the SWCNT source.

Estimation of optimal number of grid points for triangulation

To estimate an optimal number points to use in triangulation grid scans, we first measured emission from a localized SWCNT source under a 5 mm tissue phantom using a 16 x 16 point grid with 1 s per point acquisition time. We then wrote a LabVIEW program to randomly select different subsets from the data containing between 3 and 250 points, and the location of the SWCNT source was deduced with each subset by spectral triangulation. The distance error in each case was calculated by subtracting the deduced location from the actual location. For each sampling number, we repeated the same random sampling 1000 times and averaged to obtain an expected error distance. Figure S12 shows a semi-log plot of these expected errors vs. sampling number. As the number of points increases, there is an initial sharp drop in error followed by a regime of much slower improvement. A reasonable estimate for an efficient number of sampling points is given by the intersection of lines through these regimes, or about 14 points. This choice gave position errors smaller than 0.1 mm.

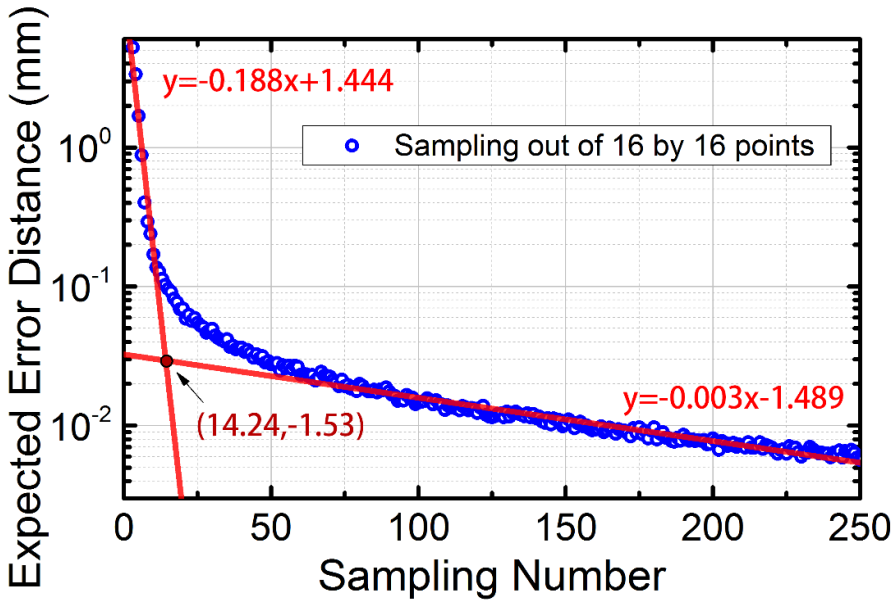

Figure S12. Estimation of the appropriate number of data points by calculating expected error distance with various sampling number.

Estimation of optimal number of grid points with constrained total acquisition time

The precision of spectral triangulation will depend not only on the number sampled grid points but also on the total acquisition time, which may be a constrained experimental parameter. We therefore examined relative errors as a function of number of points with a fixed acquisition time divided equally among them. Figure S13 shows the position error with respect to number of data points. Three measurements were performed with each number of data points. Similar position errors were found when the number of points was between 9 and 25, but the error was greater using only 4 points and probably also with 36. An optimum range seems to be 10 to 30 points.

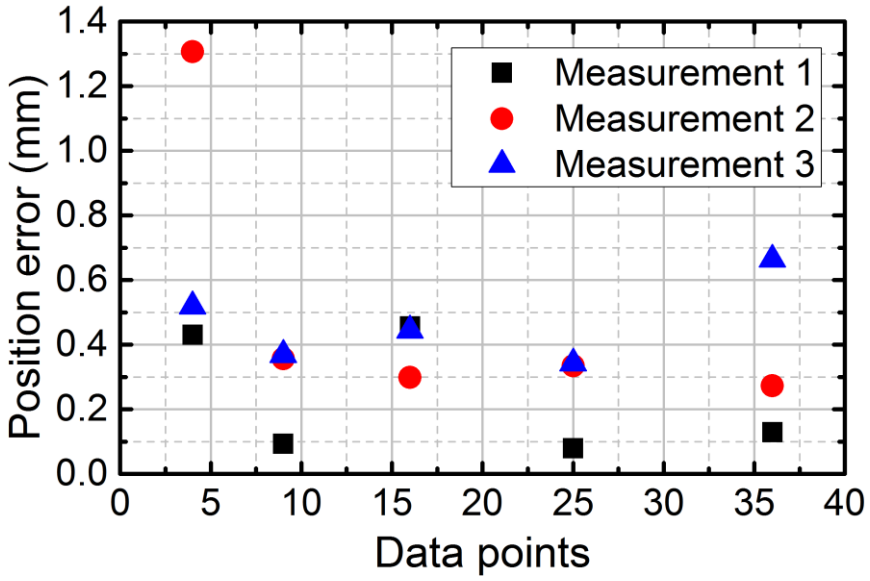

Figure S13. Calculation of position errors between spectrally triangulated and actual SWCNT position with fixed total acquisition time.

Raw data of Figure 5

In this experiment, every set of data was measured five times in order to estimate the standard error. There are three parameters: x, y, and z, and the SWCNT source location was measured by the standard calibration procedure described in previous section.

Table S1. Raw data of Figure 5

SWCNT Depth (mm)	Data set	Position (simulated)		
		x	y	z
3.58 mm	1	73.5104	74.9522	7.22138
	2	73.5142	74.937	7.19222
	3	73.5943	74.9301	7.1993
	4	73.6254	74.9124	7.17452
	5	73.6505	74.9391	7.18918
6.70 mm	1	73.493	75.0437	7.45802
	2	73.5332	75.0089	7.34355
	3	73.5766	74.8875	7.36886
	4	73.6233	74.9444	7.24733
	5	73.5859	74.9087	7.15516
9.65 mm	1	73.4227	75.3915	6.68656
	2	73.4396	75.2942	6.90612
	3	73.4973	75.1063	6.82787
	4	73.4157	75.1406	6.8736
	5	73.5338	75.0975	7.2473
Actual location of SWCNT		73.455	74.855	7.170

Table S2. Data of Figure 5

depth (mm)	Δx mean	Δx std	Δy mean	Δy std	Δz mean	Δz std
3.582	0.124	0.064	0.108	0.050	3.59	0.051
6.703	0.079	0.015	0.104	0.066	7.05	0.131
9.647	0.025	0.017	0.145	0.117	9.39	0.207

Evaluation of the fit quality

In Figure 5, we showed that the triangulated positions were very close to the actual positions. Here in Figure S14, we want to check the quality of the acquired data and also how consistent it is with the attenuation curve. The closest points at around 4.5 mm were ignored because intensity predictions from diffusion theory show errors at shorter distances. Less random noise was present with thinner tissue phantoms, thicker phantoms led to more random noise in the data. Despite this noise, there were enough data points to accurately predict the slopes of the attenuation curves. Their consistency validates the spectral triangulation analysis.

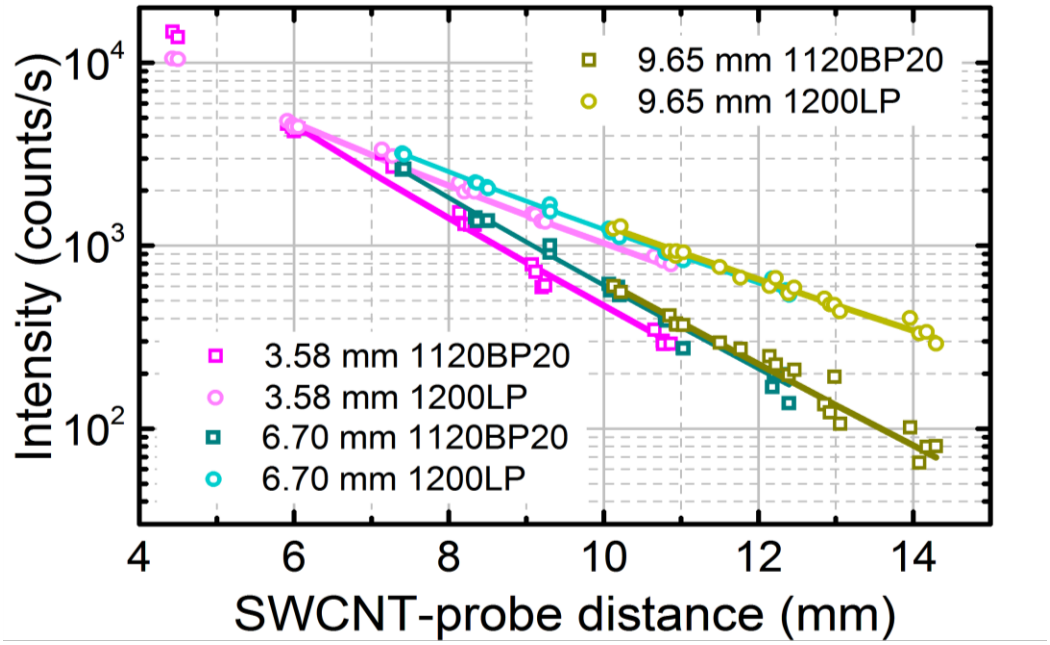

Figure S14. Plot of measured intensities and their corresponding fitted curves. Square and round points represent the intensities measured with 1120 nm band pass filter and 1200 nm long pass filter, respectively. Line curves represent the fitted curve in spectral triangulation. The three colors represent different phantom thicknesses (3.58, 6.70, and 9.65 mm)

Simulation of surface fluorescence profile of two SWCNT sources

Light scattering degrades the resolution of images of SWCNT fluorescence sources acquired through tissues. If the source is two separate emitters, they can become indistinguishable and appear as one in the image. In Figure S15, two SWCNT sources are separated 5 mm apart. We simulated the surface fluorescence profiles through various thicknesses of tissue phantom using experimental attenuation coefficients. Two resolvable sources are observed in profiles through 1

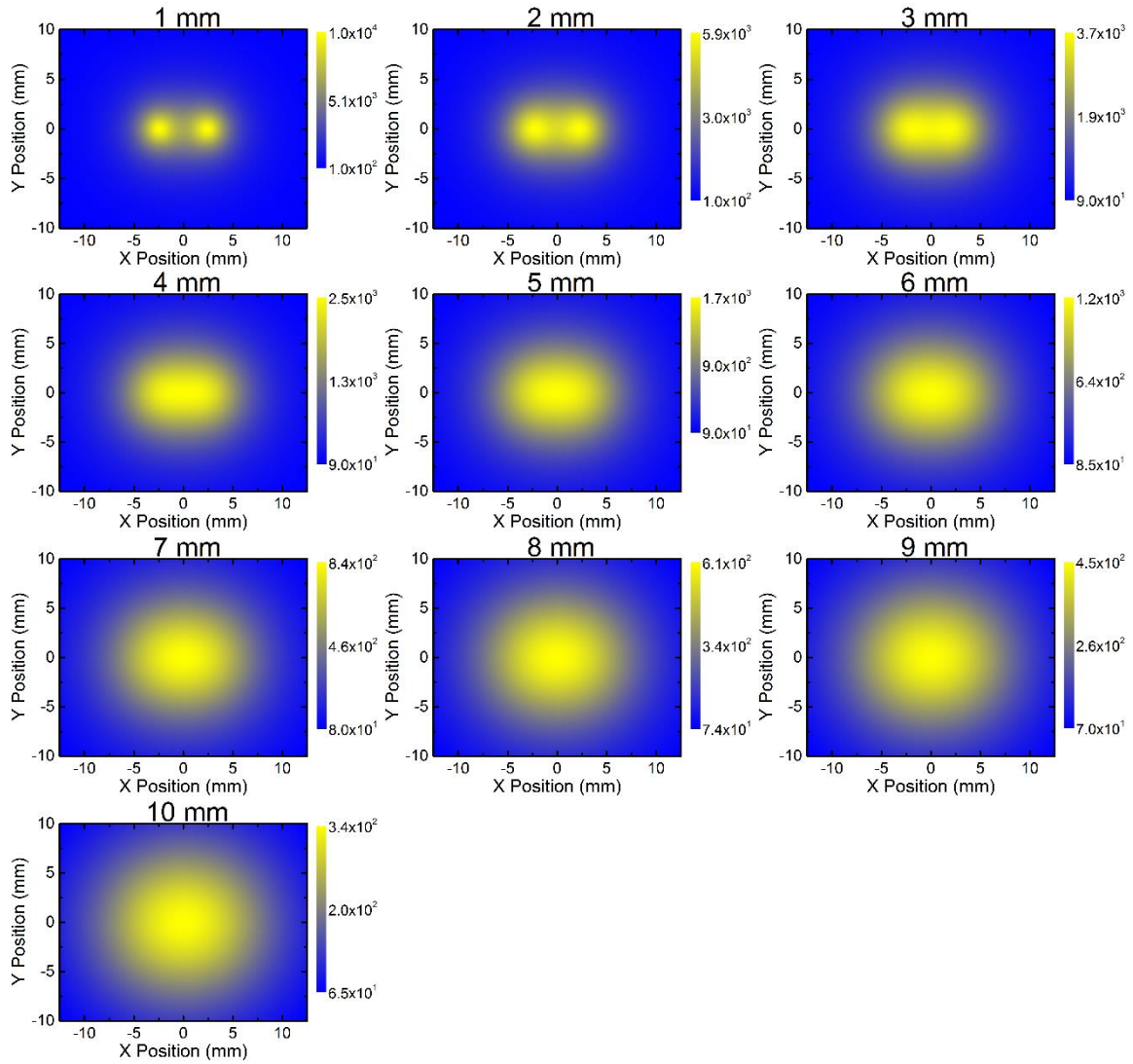

Figure S15. Simulation of surface profile of two SWCNT sources (1120 nm long pass filter) with various thicknesses of tissue phantoms.

and 2 mm thicknesses, but not through thicker phantoms. The thicker tissue phantoms lead to the collection of more scattered than unscattered photons by our probe, blurring the spatial information in the image. By contrast, a conventional imaging camera with smaller aperture can collect a higher fraction of unscattered photons and thus slightly better spatial resolution, but with much lower sensitivity. Our spectral triangulation method can resolve dual SWCNT sources despite their blurred surface profiles because of the wavelength dependence of those profiles. Therefore, spectral triangulation provides a new way to analyze fluorescence sources deeper inside turbid media.

Generalized spectral triangulation analysis

We will use the index $i = 1, 2, \cdots, i_{\max}$ to label different probe measurement positions $\mathbf{r}_i$, index $j = 1, 2, \cdots, j_{\max}$ will label different localized emission sources at positions $\mathbf{r}_j$, and index $k = 1, 2$ will label the two different spectral filter ranges. The measured fluorescence signal at position $\mathbf{r}_i$ with filter k is then denoted $I_{i,k}^{\exp}$ and the distance between source j and probe position i is $d_{ij} = \left|\mathbf{r}_j - \mathbf{r}_i\right|$. The fluorescence signal at position $\mathbf{r}_i$ through filter k predicted by our model is the sum over contributions from all sources: $I_{i,k}^{\text{model}} = \sum_{\substack{\text{sources} \\ j=1}}^{j_{\max}} \alpha_{j,k} I^{\text{model}}\left(\lambda_k, d_{ij}\right)$, where each term in the sum involves a coefficient $\alpha_{j,k}$ that reflects the emission strength of source j in spectral band k. The sum of squared residuals (*SSR*) between the experimental and modeled intensities is given by

$$SSR\left\{\mathbf{r}_j\right\} = \sum_{\substack{\text{filters} \\ k=1}}^{2} \sum_{\substack{\text{probes} \\ i=1}}^{i_{\max}} \left[I_{i,k}^{\exp} - \sum_{\substack{\text{sources} \\ j=1}}^{j_{\max}} \alpha_{j,k} I^{\text{model}}\left(\lambda_k, d_{ij}\right) \right]^2$$

Here, $I_{j,i,k}^{\text{model}} = I^{\text{model}}\left(\lambda_k, d_{ij}\right) \propto e^{-\mu(\lambda_k) d_{ij}} / d_{ij}$, where $\mu\left(\lambda_k\right)$ is the experimental wavelength-dependent attenuation coefficient.

At each set of source positions $\left\{\mathbf{r}_j\right\}$, we analytically minimize *SSR* with respect to the variables $\alpha_{j,k}$. At the extremum,

$$\frac{\partial}{\partial \alpha_{l,k}} \left\{ \sum_{k=1}^{2} \sum_{i=1}^{i_{\max}} \left[I_{i,k}^{\exp} - \sum_{j=1}^{j_{\max}} \alpha_{j,k} I_{j,i,k}^{\text{model}} \right]^2 \right\} = 0 .$$

where $l = 1, 2, \cdots, j_{\max}$ refers to a specific source. Evaluating gives the relations

$$\sum_k \sum_j \left[\left(\sum_i I_{l,i,k}^{\text{model}} I_{j,i,k}^{\text{model}} \right) \alpha_{j,k} \right] = \sum_k \sum_i I_{i,k}^{\text{exp}} I_{l,i,k}^{\text{model}}$$

This can be expressed as a matrix linear equation: $\mathbf{A}_k \alpha_k = \mathrm{b}_k$, where $\mathbf{A}_k$ is a symmetric matrix and α_k is the target solution vector of intensity factors:

$$\mathbf{A}_k = \begin{pmatrix} \sum_i I_{1,i,k}^{\text{model}} I_{1,i,k}^{\text{model}} & \cdots & \sum_i I_{1,i,k}^{\text{model}} I_{j,i,k}^{\text{model}} \\ \vdots & \ddots & \vdots \\ \sum_i I_{1,i,k}^{\text{model}} I_{j,i,k}^{\text{model}} & \cdots & \sum_i I_{j,i,k}^{\text{model}} I_{j,i,k}^{\text{model}} \end{pmatrix}_{jj} , \quad \mathrm{b}_k = \begin{pmatrix} \sum_i I_{1,i,k}^{\text{exp}} I_{1,i,k}^{\text{model}} \\ \vdots \\ \sum_i I_{1,i,k}^{\text{exp}} I_{j,i,k}^{\text{model}} \end{pmatrix}_j$$

We solve for the vector α_k for each filter (*k*) independently using the Lawson-Hanson non-negative least square (NNLS) numerical method, since intensities must be non-negative. The result is used to compute the optimized value of total *SSR* (the sum of *SSR* values with the two filters) for a specific set of source positions, $\{\mathbf{r}_j\}$. A Simplex algorithm then systematically varies those source positions to find the global minimum total *SSR* value. The resulting $\{\mathbf{r}_j\}$ represent the triangulated coordinates of the set of localized SWCNT emission sources that best account for the experimental optical data.

Estimation of optical coefficients of 1% tissue phantom

Tissue phantom that contains 1% Intralipid has ~ 96% water content. The water absorption coefficient at 1200 nm is 0.127 mm^{-1}. Hence, the water absorption at 1200 nm can be estimated to be 0.12 mm^{-1}. Troy et al. estimated the ratio of isotropic scattering coefficient to absorption coefficient (μ_s'/μ_a) of 1% Intralipid tissue phantom to be ~7 at 1200 nm. Therefore, the corresponding isotropic scattering coefficient is $\mu_s' = 0.12 \times 7 = 0.85\ \text{mm}^{-1}$. The effective attenuation coefficient can be expressed as $\mu_{\text{eff}} = \sqrt{3\mu_a(\mu_a + \mu_s')}$, that is, $\mu_{\text{eff}} = \sqrt{3 \times 0.12(0.12 + 0.85)} = 0.59\ \text{mm}^{-1}$.